Research Letter

How to Cite: *J. Inorg. Mater.*, 2026, **41(5):** 663
**DOI:** 10.15541/jim20250157

# Ligand-hydroxylated UiO-66 for Enhanced Photothermally Catalytic VOCs Oxidation

CHEN Xiaochen[1,2], WANG Yang[2], YANG Bin[1], WANG Min[2], A Bohan[2], WANG Man[2], ZHANG Lingxia[1,2]

(1. School of Chemistry and Materials Science, Hangzhou Institute for Advanced Study, University of Chinese Academy of Sciences, Hangzhou 310024, China; 2. Shanghai Institute of Ceramics, Chinese Academy of Sciences, Shanghai 200050, China)

**Abstract:** The efficient removal of low-concentration volatile organic compounds (VOCs) in indoor and industrial environments remains a significant challenge. Metal-organic frameworks (MOFs) are potential oxidation catalysts due to their superior adsorption enrichment capability for low-concentration VOCs. In this work, hydroxyl-containing ligands were introduced into UiO-66, and the as-synthesized UiO-66-OH catalyst exhibited exceptional photothermal catalytic performance on oxidation of flowing low-concentration VOCs (initial concentrations of 0.075 mg/L for toluene and 0.064 mg/L for benzene, a weight hourly space velocity (WHSV) of 30000 mL/(g·h)), achieving 97% and 90% conversion of toluene and benzene, respectively, surpassing the reported photothermal catalysts such as metal oxides and noble-metal-loaded catalysts. Such impressive activity is attributed to the synergy of thermal catalysis and photocatalysis. Ligand hydroxylation optimizes the electron structure and the ligand-to-metal charge transfer (LMCT) effect, enhancing light absorption, improving electron-hole separation efficiency and photothermal properties of UiO-66. Hydroxyl introduction promotes the formation of oxygen vacancies, facilitating oxygen adsorption/activation to sustain lattice oxygen ($O_{latt}$) and generate superoxide radical ($\cdot O_2^-$), which are the dominant reactive species in VOCs oxidation. This work not only presents the potential of MOFs as efficient photothermal catalysts for the oxidation of low-concentration VOCs but also shows prospects on facile modulation of electron structure by ligand engineering to enhance the photothermal properties of MOFs.

**Key words:** volatile organic compound; low concentration; metal-organic framework; photothermal catalysis; ligand-to-metal charge transfer effect

Accelerated urbanization and industrial activities have significantly increased VOC emissions, which are major contributors to air pollution and pose serious health risks, including respiratory and neurological damage[1]. As precursors to ozone and smog, VOCs significantly impact global air quality[2]. Catalytic oxidation is an effective approach to eliminate VOCs by converting them into harmless $CO_2$ and $H_2O$. While thermocatalysis is efficient for high-concentration VOCs, it requires elevated temperatures[3]. In contrast, photocatalysis works at ambient conditions and suits low-concentration VOCs but suffers from limited efficiency. Thus, achieving rapid and effective low-temperature removal of dilute VOCs remains a key challenge.

Photothermal catalysis combines the strengths of thermo- and photocatalysis, using solar energy to enhance low-temperature activity and thermal oxidation, offering superior performance over either method alone[4]. Photothermal catalysts for VOCs oxidation mainly include metal oxides and noble-metal-loaded semiconductors. Metal oxides such as $Co_3O_4$ offer structural stability and dual activation in virtue of thermal or light energy. Meanwhile, noble metals (*e.g.*, Pt, Au) enhance light absorption and accelerate reaction kinetics through

**Received date:** 2025-04-13 **Revised date:** 2025-06-26; **Published online:** 2025-07-31
**Foundation item:** National Natural Science Foundation of China (22405287); Science and Technology Commission of Shanghai (24DZ2201600, 24ZR1475800); China Postdoctoral Science Foundation (2024M760699)
**Biography:** CHEN Xiaochen (1999–), male, Master candidate. E-mail: chenxiaochen22@mails.ucas.ac.cn
陈笑晨(1999–), 男, 硕士研究生. E-mail: chenxiaochen22@mails.ucas.ac.cn
**Corresponding author:** ZHANG Lingxia, professor. E-mail: zhlingxia@mail.sic.ac.cn
张玲霞, 研究员. E-mail: zhlingxia@mail.sic.ac.cn

localized surface plasmon resonance (LSPR) effects, significantly improving catalytic efficiency[5]. Despite substantial advancements in photothermal catalysis for VOCs removal, most research focus on moderate to high-concentration VOCs (0.5–10 mg/L), relevant to industrial emissions, and may not effectively address low-concentration VOCs (<0.1 mg/L) critical to indoor and ambient air quality.

Metal-organic frameworks (MOFs) featured with high specific surface area, adjustable porosity, and abundance of active sites, exhibit excellent adsorption capability for VOCs, enabling them to effectively concentrate low-concentration VOCs. Ma *et al*.[6] synthesized Fe-based MOFs (MIL-100(Fe), MIL-101(Fe), MIL-53(Fe)) for toluene adsorption, with MIL-100(Fe) showing the highest capacity (663 mg/g). Its performance stems from π-π interactions between toluene and the ligand, and efficient pore filling *via* its hierarchical structure. Chen *et al*.[7] designed a cobalt-adeninate MOF (MOF-11), which demonstrated a saturated adsorption capacity up to 0.73–3.57 mmol/g following the order of toluene< benzene<acetone<methanol. As photocatalysts, current MOFs remain mediocre due to their limited light-harvesting capability and poor charge separation efficiency, often addressed by combining them with metal oxides or other semiconductors. Lv *et al*.[8] synthesized MOF@COF heterojunction to improve light absorption, accelerate charge transfer and extend electron-hole pair lifetime, achieving improved visible-light-driven VOCs oxidation performance. Zhang *et al*.[9] developed $TiO_2$/UiO-66-$NH_2$ nanocomposites, which achieved 72.7% and 70.74% conversion of toluene and acetaldehyde, respectively, under flowing conditions with initial concentrations of 0.094 mg/L for toluene and 0.044 mg/L for acetaldehyde under the irradiation of a 50 mW/cm$^2$ mercury lamp. However, most reports on MOFs-based materials for VOCs oxidation focus on photocatalysis and scarcely involve photothermal catalysis.

LMCT, which involves electrons excited from ligand orbitals to metal center, is a fundamental effect in coordination complex or MOFs. By introducing new charge transfer states and altering electronic structure, LMCT effect can be modulated to extend the light absorption of catalysts to visible range. Moreover, LMCT could improve charge separation and mobility, thereby reducing electron-hole recombination, which is critical for efficient photocatalysis. As reported by theoretical calculations in an early study[10], LMCT in MOFs is closely related to the characteristics of metal and ligand, which can be systematically modulated by introducing electron-donating or electron-withdrawing functional groups, such as –OH and –$NH_2$, into ligands.

Despite the promising potential of MOFs in the removal of low-concentration VOCs, their intrinsic photothermal catalytic performance remains limited. In this work, UiO-66 was selected as the base material, and a ligand modification strategy was employed to regulate LMCT effect. By introducing functional groups, the light absorption capability, charge separation efficiency, and overall photothermal catalytic activity of UiO-66 were significantly enhanced. Furthermore, the possible mechanism behind the superior photothermal performance of UiO-66-OH was proposed. This study highlights an effective ligand engineering strategy to improve the photothermal effect of MOFs and their potential as highly efficient and stable photothermal catalysts for low-concentration VOCs oxidation.

# 1 Experimental

The functionalized Zr-based MOFs, abbreviated as UiO-66-X (X=$NO_2$, $NH_2$, OH, NDC) were synthesized following the reported method (Fig. 1(a))[11].

Specifically, 1 mmol of $ZrCl_4$ was dissolved in 30 mL of dimethylformamide (DMF) and 2 mL of concentrated hydrochloric acid. 1 mmol of ligand (2-hydroxyterephthalic acid (–OH), 2-nitroterephthalic acid (–$NO_2$), 2-aminoterephthalic acid (–$NH_2$), 2,6-naphthalenedicarboxylic acid (–NDC), and terephthalic acid) was dissolved in 30 mL of DMF. Subsequently, two solutions were mixed and placed in an 80 mL Teflon-lined stainless-steel autoclave and heated under certain conditions (Table S1). After cooling to room temperature, the solid product was filtered and thoroughly washed several times with DMF and ethanol, then dried overnight at 60 ℃ under vacuum. To enhance purity, the dried powder was dispersed in 60 mL of ethanol and stirred for 24 h, filtered, and dried again overnight at 60 ℃ under vacuum, yielding the final MOF product.

Experimental details are provided in the Supporting Materials.

# 2 Results and discussion

## 2.1 Structure and composition

X-ray diffraction (XRD) patterns illustrate the phase structure and crystallinity of all five catalysts (Fig. 1(b)). All catalysts exhibit characteristic diffraction peaks at $2\theta$=7.3°, 8.4° and 25.4° corresponding to the (111), (002), and (006) crystal planes of UiO-66, respectively. This verifies that the structural integrity has been well maintained after the introduction of different ligands.

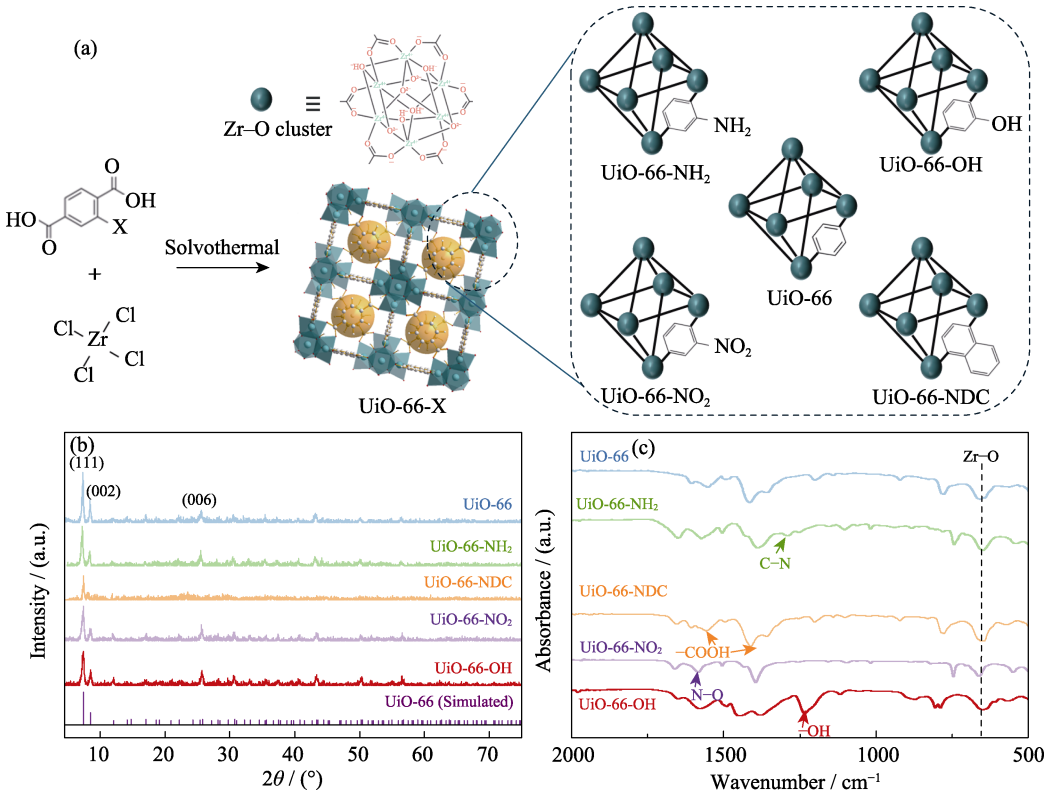


Fig. 1　(a) Schematic diagram of the synthesis procedure, (b) XRD patterns and (c) FT-IR spectra of UiO-66 and UiO-66-X

Compared to pristine UiO-66, the diffraction intensities of (111), (002), and (006) planes of the UiO-66-X samples decrease, indicating a decrease in long-range structural order after ligand modification[11]. Among them, UiO-66-NDC exhibits the most significant intensity decline, which can be attributed to steric hindrance and π-π stacking interactions that disrupt the regular coordination environment and lead to structural distortion.

Fourier transformed infrared (FT-IR) spectra reveal the introduction of functional groups (Fig. 1(c)). For UiO-66-$NH_2$, the absorption bands at 3360 and 3467 $cm^{-1}$ correspond to the symmetric and asymmetric N–H stretching vibrations of primary amine groups (Fig. S1)[12] and the band at 1290 $cm^{-1}$ corresponds to the C–N bonds of aromatic amines[12]. For UiO-66-NDC, the absorption bands located at 1410 and 1556 $cm^{-1}$ represent the symmetric and asymmetric stretching vibrations of –COOH group in the NDC linker[13], respectively. UiO-66-$NO_2$ shows the N–O vibration band of –$NO_2$ group at 1580 $cm^{-1}$[14], and a distinct –OH band at 1233 $cm^{-1}$ exists in UiO-66-OH[14-15]. All samples show a distinct bending absorption band of Zr–O cluster at 650 $cm^{-1}$[15].

## 2.2　Photothermal catalytic performance

The photothermal catalytic activities of the catalysts for oxidation of toluene and benzene were evaluated in a continuous flow reactor. The initial concentration of toluene and benzene was 0.075 and 0.064 mg/L, respectively. UiO-66-X materials exhibit enhanced photothermal catalytic performance compared to pristine UiO-66, and UiO-66-OH exhibits the highest activity. For toluene oxidation, UiO-66-OH achieves a stable maximum conversion up to 97% within 20 min, significantly outperforming pristine UiO-66, whose toluene conversion is only 60% following a subsequent decline (Fig. 2(a)). Similar trends can also be observed in benzene oxidation, where UiO-66-OH achieves a conversion rate of 90% within 10 min and sustains high activity over the extended reaction time, compared to the lower benzene conversion rate below 50% on UiO-66 (Fig. 2(b)). To evaluate the superiority of UiO-66-OH catalyst over conventional photothermal catalysts, a comparison is listed in Table S2. The reports closely matching the experimental conditions of this work were chosen, including the type of reactor, light intensity, *etc*. Notably, despite the absence of noble metals or heterogeneous components, UiO-66-OH achieves conversion levels of toluene and benzene comparable to or higher than those reported catalysts in the literature, demonstrating the high effectiveness and potential of MOF-based materials for photothermal catalytic oxidation of VOCs.

The cyclic performance on photothermal catalytic oxidation of both toluene and benzene demonstrates the robustness of UiO-66-OH (Figs. 2(c, d)). Across five cycles, UiO-66-OH retains its high conversion efficiency

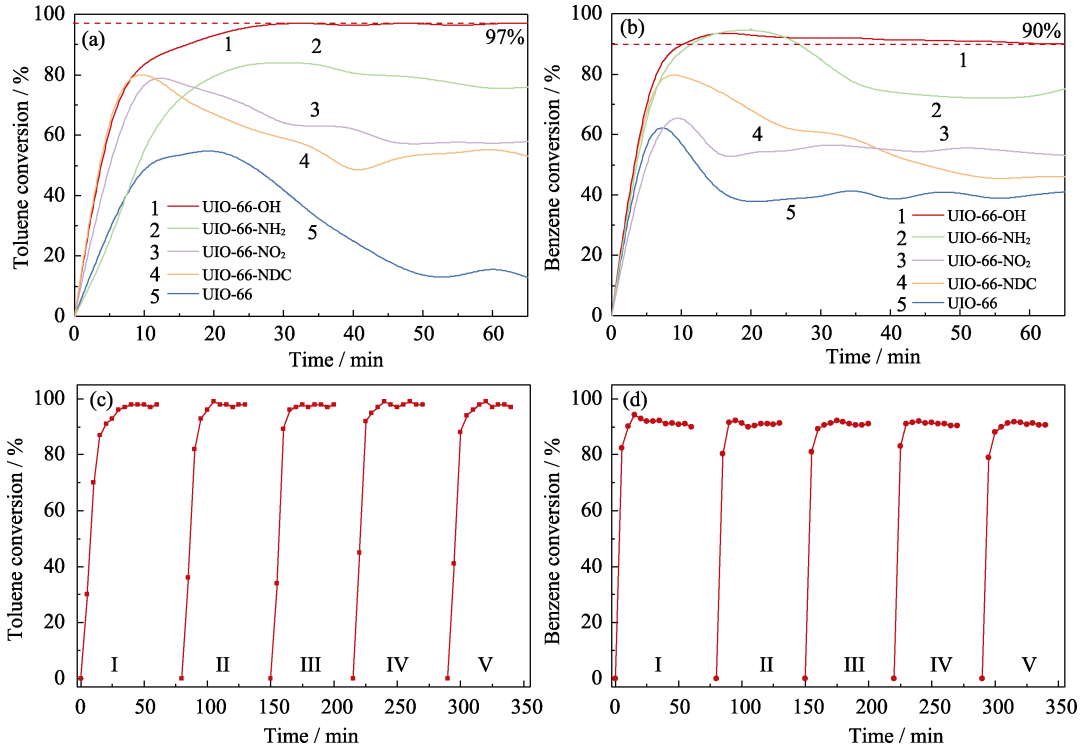


Fig. 2 (a, b) Photothermal catalytic performance of UiO-66-X and UiO-66 for oxidation of (a) toluene and (b) benzene, and (c, d) cycle stability of UiO-66-OH for photothermal catalytic oxidation of (c) toluene and (d) benzene

without noticeable deactivation, with toluene and benzene conversion remaining ~95% (Fig. 2(c)) and ~90% (Fig. 2(d)), respectively, emphasizing its stability under prolonged operational conditions. Scanning electron microscopy (SEM) images of UiO-66-OH before (Fig. S2(a)) and after (Fig. S2(b)) five cycles demonstrate that the material retains uniform morphology and well-defined particle structure, with no observable changes, indicating excellent morphological stability of UiO-66-OH. XRD pattern of UiO-66-OH after five cycles (Fig. S2(c)) shows no significant changes compared to the fresh sample, further confirming the material's outstanding structural robustness and crystallographic stability throughout the catalytic process.

$N_2$ adsorption-desorption isotherms of UiO-66 and UiO-66-OH collected at 77 K (Fig. S3) exhibit typical type I behavior, characteristic of microporous materials. UiO-66 shows a high specific surface area of 1198 $m^2/g$. After hydroxyl functionalization, the specific surface area of UiO-66-OH decreases to 855 $m^2/g$, which can be attributed to partial pore occupation by the introduced –OH groups. Both materials possess dominant pore sizes corresponding to the tetrahedral cages (~8.3 Å) and the octahedral cages (~13 Å), which well match the molecular kinetic diameters of benzene (5.03 Å) and toluene (5.35 Å)[16]. This size compatibility suggests that UiO-66 frameworks can effectively adsorb and transport VOCs molecules, thereby facilitating their rapid catalytic conversion.

## 2.3 Electron structure and photothermal property

The photothermal conversion capabilities of the catalysts were evaluated. Under Xe lamp irradiation with a light intensity of 300 $mW/cm^2$, the equilibrium surface temperatures of the samples were measured. The results indicate that different ligands significantly influence the photothermal conversion properties of UiO-66-X. As shown in Fig. 3(a), UiO-66-$NH_2$ reaches an equilibrium temperature of 155 ℃ within 5 min, exhibiting the highest photothermal conversion efficiency. Followed by UiO-66-OH, which achieves a stable temperature of 130 ℃ after 15 min. Whereas UiO-66-$NO_2$ and UiO-66-NDC only show slight enhancement in photothermal conversion. The photothermal enhancement effect is closely related to the ligand variety, following the order of –$NH_2$>–OH>–$NO_2$>–NDC. Based on this ordering, it can be inferred that the electron-donating ligands could induce high photothermal conversion efficiency, likely due to their enhanced light absorption, charge transfer, and nonradiative energy dissipation[17]. To verify these, UV-Vis spectroscopy, photoluminescence (PL) spectroscopy, electrochemical impedance spectroscopy and photocurrent response were conducted[18].

UV-Vis spectrum of UiO-66-OH (Fig. S4(a)) exhibits a distinct red shift of absorption edge from 346 nm of pristine UiO-66 to 377 nm, suggesting a narrowed band

gap and enhanced visible light absorption ability. Tauc plots (Fig. S4(b)) reveal a band gap reduction from 3.20 eV of UiO-66 to 2.89 eV of UiO-66-OH, which lowers the energy required for electron excitation and enables more effective charge carrier generation under visible light. This red shift and narrowed band gap lower the initial energy barrier for LMCT[19], implying that the LMCT effect is more favorable in UiO-66-OH. These improvements likely stem from electronic structure modifications introduced by hydroxyl groups, which act as electron-donating substituents, creating localized electronic states that facilitate charge separation and reduce recombination rates of photogenerated charge carriers[20]. This finding aligns with a previously published calculation study, which demonstrated that incorporating hydroxyl groups into Ce-UiO-66 resulted in a decreased LMCT energy of –1.61 eV from –1.43 eV, indicating enhanced LMCT effect due to ligand hydroxylation[10].

Mott-Schottky analysis gives more detailed energy band structure. For pristine UiO-66, the conduction band (CB) and valence band (VB) locate at −0.55 V (*vs.* SHE) and +2.65 V (*vs.* SHE) (Fig. S4(c)), respectively, corresponding to its band gap of 3.20 eV. In contrast, UiO-66-OH exhibits the CB at +0.16 V (*vs.* SHE) and the VB at +3.05 V (*vs.* SHE) (Fig. S4(d)), resulting in its reduced band gap of 2.89 eV. The CB and VB of UiO-66-OH are favorably aligned with the oxidation potentials of toluene and benzene (Fig. 3(b)). Specifically, its VB is sufficiently positive to oxidize toluene (+2.50 V) and benzene (+2.72 V)[21], indicating that the photogenerated holes in UiO-66-OH enable the direct oxidation of toluene and benzene into $CO_2$. Meanwhile, PL spectra (Fig. S5(a)) show lower fluorescence intensity of UiO-66-OH than pristine UiO-66, suggesting a suppression of radiative recombination of photogenerated charge carriers or an enhancement on charge separation.

As shown in photocurrent response spectra (Fig. S5(b)), UiO-66-OH generates a much higher and more stable photocurrent, manifesting the improved charge generation, separation, and transfer after hydroxyl introduction. Nyquist plots (Fig. S5(c)) show that UiO-66-OH has a smaller arc radius than UiO-66, signifying lowered charge transfer resistance and enhanced electron mobility after hydroxyl introduction.

Based on the above results, it can be concluded that the introduction of hydroxyl groups with strong electron-donating ability into ligands of UiO-66 effectively modulates the LMCT effect, resulting in narrowed band gap and enhanced electron transfer from ligand to metal site. Consequently, the light adsorption ability and the photocurrent response of the catalyst are effectively improved. Meanwhile, the irradiation recombination of electrons and holes is suppressed, and the photothermal property related to non-irradiation recombination is markedly elevated. Notably, the deepened VB level of UiO-66-OH endows the catalyst with strengthened oxidation capability, which is favorable for VOCs degradation.

## 2.4 Chemical composition

The chemical states of surface elements were analyzed by X-ray photoelectron spectroscopy (XPS). As shown in Figs. S6(a, b), both catalysts show $Zr^{4+}$ peaks at 182.8 ($Zr3d_{5/2}$) and 185.3 eV ($Zr3d_{3/2}$)[22], alongside $Zr^{3+}$ peaks at 181.4 ($Zr3d_{5/2}$) and 184.6 eV ($Zr3d_{3/2}$)[23]. Notably, the $Zr^{3+}$/Zr ratio increases from 16.58% of UiO-66 to 19.41% of UiO-66-OH. Since $Zr^{4+}$ can capture electrons from oxygen vacancies and be reduced to $Zr^{3+}$, the increased $Zr^{3+}$/Zr ratio suggests that the introduction of hydroxyl groups in the UiO-66 frameworks is accompanied by the generation of oxygen vacancies. O1s XPS spectra (Fig. 3(c)) show UiO-66-OH has three peaks at 530.4, 531.7, and 532.3 eV, which can be assigned to Zr–O in metal clusters, carboxylic acid groups C=O in linkers, and O–H of ligands and adsorbed water, respectively[24]. Compared to pristine UiO-66, the binding energy of adsorbed oxygen in UiO-66-OH exhibits a shift toward lower energy, which can be attributed to the band bending effect induced by oxygen vacancies within the lattice, further indicating the presence of oxygen vacancies[25].

Electron paramagnetic resonance (EPR) was implemented to confirm the existence of oxygen vacancies. Fig. S6(c) provides direct evidence for the presence of oxygen vacancies. UiO-66-OH exhibits a prominent signal with a $g$ value of 2.006, characteristic of unpaired electrons localized at oxygen vacancies[26]. Both materials show $Zr^{3+}$ signals at $g$=1.980[27], with UiO-66-OH displaying a marginally higher signal intensity compared to UiO-66. This observation aligns with the XPS analysis.

## 2.5 Mechanism of photothermal catalysis

To differentiate the individual contributions of photocatalysis and thermal catalysis during the oxidation reaction, thermocatalytic performance tests were conducted at the equilibrium temperatures mentioned above to compare with photothermal catalytic performance. The catalyst amount, benzene concentration and flow rate in thermal catalysis were kept consistent with those in photothermal catalysis to ensure valid comparison. As shown in Fig. S6(d), an enhancement of 55.4% on toluene conversion is achieved by photothermal catalysis compared with thermal catalysis, and an enhancement of 51.0% on benzene conversion is achieved. These results highlight

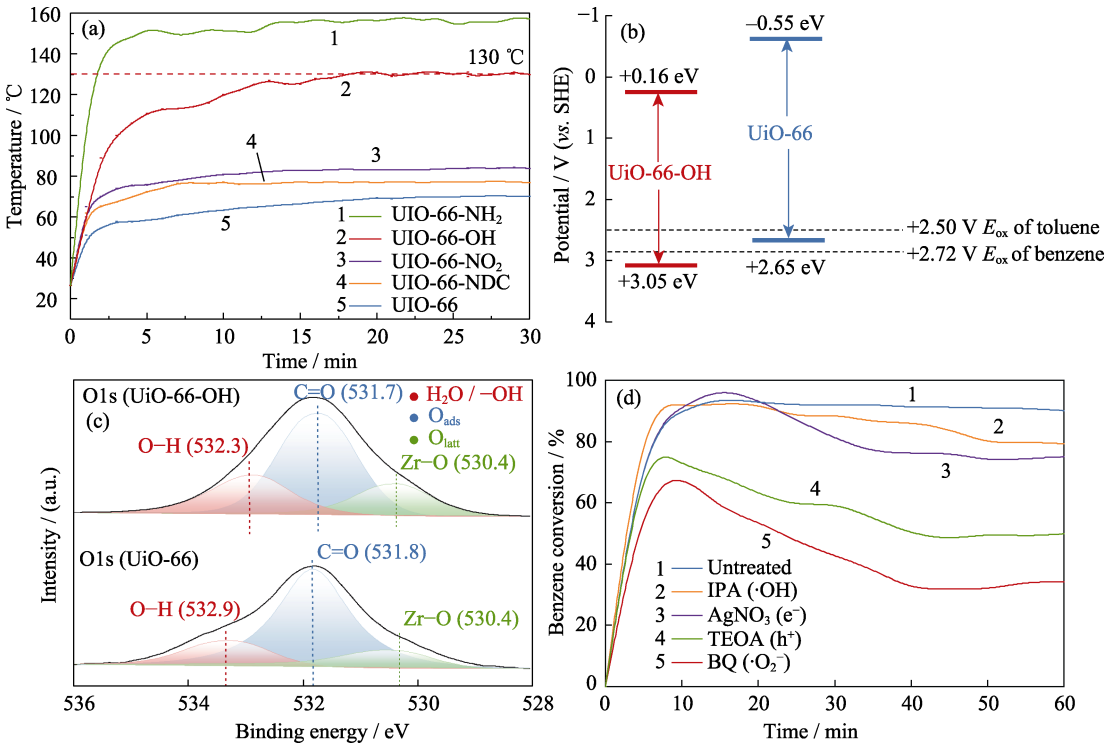


Fig. 3 (a) Surface temperature of the catalysts, (b) schematic band structure, (c) O1s XPS spectra, and (d) active species trapping experiments of UiO-66-OH

photothermal catalytic activity is not only attributed to thermal effects but also related to light-driven processes.

To probe the active species in the photothermal catalytic oxidation of VOCs over UiO-66-OH, a series of trapping experiments were conducted. Specifically, scavengers including isopropanol (IPA), $AgNO_3$, triethanolamine (TEOA), furfuryl alcohol (FFA) and benzoquinone (BQ) were used to trap hydroxyl radical (·OH), photogenerated electron ($e^-$), photogenerated hole ($h^+$), singlet oxygen ($^1O_2$) and superoxide anion ($\cdot O_2^-$), respectively. As shown in Fig. 3(d), trapping $\cdot O_2^-$ with BQ most significantly reduces benzene conversion, followed by trapping $h^+$ with TEOA, indicating that $\cdot O_2^-$ and $h^+$ are primary reactive species driving the catalytic oxidation reaction. Trapping $^1O_2$, $e^-$ and ·OH also affect conversion but to a lesser extent, suggesting that they play minor roles.

To examine the intermediates formed on the catalysts during benzene and benzene oxidation, *in-situ* FT-IR spectra were conducted under varied experimental conditions. For toluene oxidation, reaction began in light-absent and oxygen-free conditions (Fig. 4(a)). The band at 1542 $cm^{-1}$ is detected after the introduction of toluene, corresponding to C=C bond[28], representing toluene adsorbed on the surface of UiO-66-OH. As the reaction progresses, the bands at 1636 and 1681 $cm^{-1}$ gradually emerge and intensify, indicating the formation of –CHO groups[29], and signifying the oxidation of toluene to benzaldehyde. This observation demonstrates that UiO-66-OH is capable of oxidizing toluene into benzaldehyde even in the absence of light and oxygen, indicating the activity of $O_{latt}$ for toluene oxidation. In this process, benzaldehyde is identified as the first intermediate in the overall oxidation pathway. Subsequently, with the introduction of $O_2$, additional characteristic peaks appear (Fig. 4(b)). The band at 1451 $cm^{-1}$ corresponds to –COOH[30], and those at 1102 and 1264 $cm^{-1}$ correspond to –OH[31]. These suggest that benzaldehyde is further oxidized to benzoic acid and benzyl alcohol, which is most likely attributed to the supplemented $O_{latt}$ by $O_2$ activation at oxygen vacancies. However, no evidence of aromatic ring cleavage in toluene is observed under this condition, indicating that the oxidation process remains localized to the $–CH_3$ groups. When introducing light irradiation, additional characteristic bands are observed alongside those previously identified (Figs. 4(c, d)). Notably, the band at 1741 $cm^{-1}$ corresponding to maleic anhydride[32] is detected, indicating that the benzene ring structure is attacked and cleaved. Furthermore, a distinct band at 2357 $cm^{-1}$ is observed, representing $CO_2$[32], confirming that toluene completely mineralized under irradiation. This manifests that the key reactive oxidation species, $\cdot O_2^-$ and $h^+$, generated by photo excitation, are responsible for the mineralization of toluene.

For benzene oxidation, as shown in Fig. 5(a), the *in-situ* FT-IR spectra reveal a distinct C=C vibration

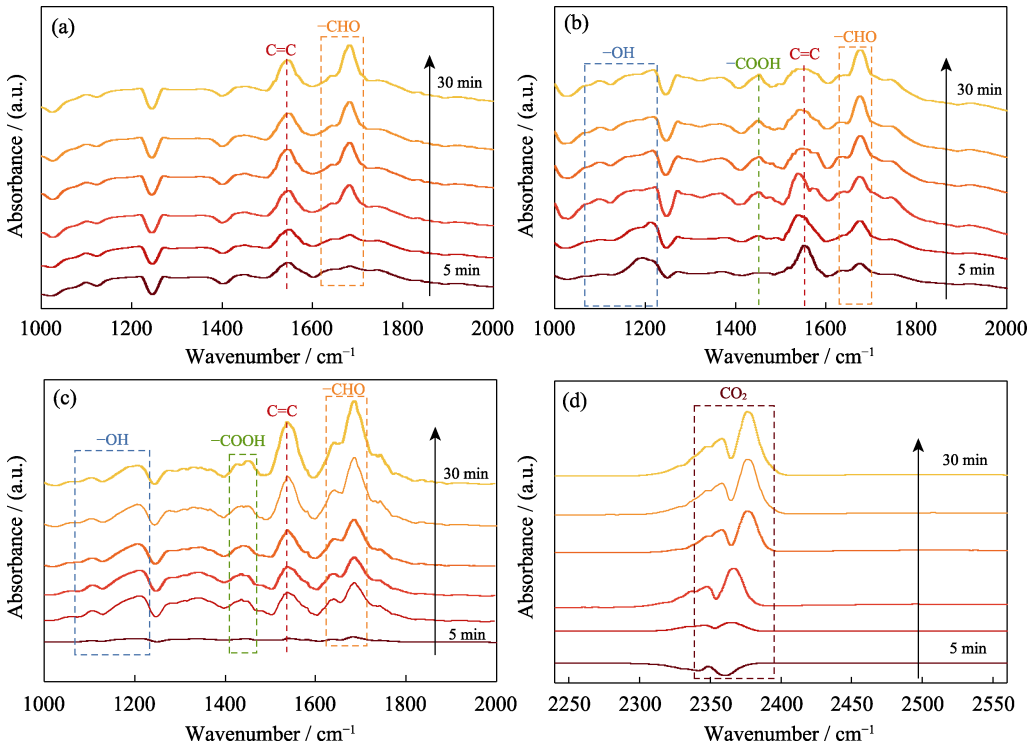


Fig. 4　*In-situ* FT-IR spectra of UiO-66-OH for oxidation of toluene under different successive conditions
(a) In dark without $O_2$; (b) In dark with $O_2$; (c, d) With $O_2$ and irradiation

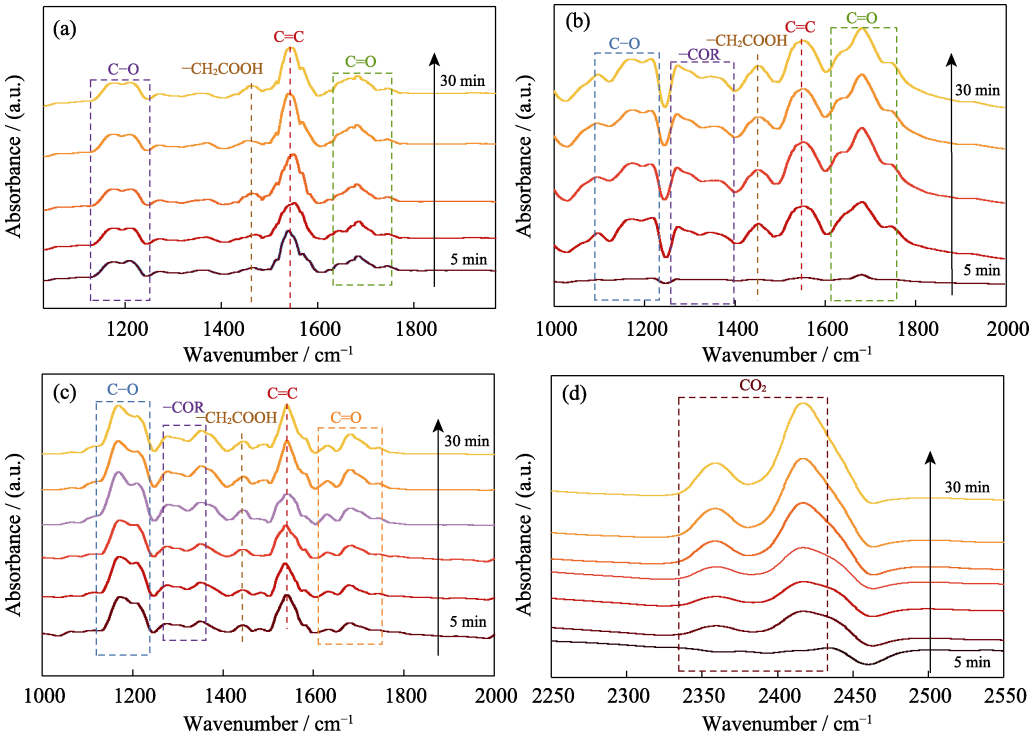


Fig. 5　*In-situ* FT-IR spectra of UiO-66-OH for oxidation of benzene under different successive conditions
(a) In dark without $O_2$; (b) In dark with $O_2$; (c, d) With $O_2$ and irradiation

band at 1543 $cm^{-1}$ corresponding to the adsorption of benzene on the surface of UiO-66-OH. Additionally, C–O vibration bands at 1170 and 1211 $cm^{-1}$ are observed, indicating the formation of phenol[33]. Furthermore, the C=O vibration band at 1683 $cm^{-1}$ suggests the presence of quinone as another intermediate. A small band at 1462 $cm^{-1}$ associated with $–CH_2COOH$ indicates partial destruction of the ring structure under the absence of light and $O_2$,

manifesting $O_{latt}$ is effective in C–H and benzene ring activation. Upon the introduction of oxygen, as illustrated in Fig. 5(b), the intensity of the bands at 1167 and 1209 $cm^{-1}$ increases significantly, indicating that phenol is the predominant intermediate. The –COR vibrational bands at 1272 and 1349 $cm^{-1}$ are characteristic of anhydrides. The band at 1462 $cm^{-1}$ corresponds to $–CH_2COOH$ persists. Under light irradiation, *in-situ* FT-IR spectra depicted in Figs. 5(c, d) reveal significant enhancements on the C=O bands at 1634, 1678, and 1747 $cm^{-1}$, indicating that quinone becomes the dominant intermediate product. The anhydride bands at 1272 and 1349 $cm^{-1}$ and the acetate band at 1462 $cm^{-1}$ are all intensified, suggesting that the benzene ring cleavage has been accelerated under light irradiation and $O_2$. Finally, distinct $CO_2$ peaks at 2353 and 2423 $cm^{-1}$ indicate that benzene undergoes complete mineralization.

*In-situ* FT-IR spectra were also conducted to investigate the catalytic behavior of pristine UiO-66 for degradation of benzene and toluene. The results indicate that even under irradiation with $O_2$, only early-stage intermediates such as benzaldehyde, benzyl alcohol, and phenol species are generated on UiO-66 (Fig. S7). The characteristic bands of these intermediates are significantly weaker and less defined compared to those on UiO-66-OH. No signals corresponding to ring-opening products or further oxidized species are detected. This suggests that pristine UiO-66 has much lower catalytic oxidation activity, which makes it difficult to completely degrade benzene and toluene.

Based on the above results, the photothermal catalysis of toluene and benzene oxidation on UiO-66-OH can be summarized as the synergy of thermal catalysis and photocatalysis. In thermal catalysis, $O_{latt}$ is involved and mainly contributes to C–H oxidation. In photocatalysis, $\cdot O_2^-$ and $h^+$ participate and are responsible for C–C cracking, aromatic ring oxidation, and finally mineralization to $CO_2$ and $H_2O$. The ligand hydroxylation leads to increased oxygen vacancies and enhanced LMCT effects in UiO-66-OH. The presence of oxygen vacancies is found to improve the activity of $O_{latt}$ and the adsorption/activation of $O_2$, thus elevating the thermal catalytic performance on VOCs oxidation. The enhanced LMCT effects result in narrowed band gaps to enhance light absorption and photothermal properties, together with promoted charge separation and transfer efficiency, boosting the generation of $\cdot O_2^-$ and $h^+$, and the photocatalytic oxidation performance. Notably, the VB level has been deepened to a strengthened oxidation direction, enhancing the oxidation ability of photogenerated $h^+$, favoring the deep mineralization of toluene and benzene. Nonradiative recombination of $e^-$ and $h^+$ produces heat, leading to the rising temperature under irradiation. The localized thermal energy promotes the activity of $O_{latt}$, the charge ($e^-$ and $h^+$) transfer and mass (reactants, intermediates and products) diffusion, boosting the overall efficiency of the oxidation reaction.

The possible pathways of photothermal catalytic oxidation of toluene and benzene on UiO-66-OH catalyst are shown in Fig. S8. Under irradiation, $e^-$ and $h^+$ are produced. Partial $e^-$ and $h^+$ recombine *via* nonradiative mode to release heat, raising the catalyst temperature and enhancing the activity of $O_{latt}$. Meanwhile, $e^-$ at CB participates in the generation of $\cdot O_2^-$. Toluene or benzene is adsorbed on the surface of catalyst and $O_2$ is activated by oxygen vacancies. For toluene oxidation, the $–CH_3$ group of toluene is attacked by surface $O_{latt}$ and stepwise oxidized to benzyl alcohol, benzaldehyde and benzoic acid. Subsequently, in virtue of $\cdot O_2^-$ and $h^+$, the ring-opening reaction takes place and produces maleates as ring-opening intermediates, which are finally transformed into $CO_2$ and $H_2O$. For benzene oxidation, the C–H bond of benzene is stepwise oxidized by surface $O_{latt}$ to phenol and quinone. Then $\cdot O_2^-$ and $h^+$ attack the aromatic ring, and ring-opening intermediates such as acetic acid and acetic anhydride are produced stepwise and finally mineralized into $CO_2$ and $H_2O$.

## 3 Conclusions

In this work, a series of UiO-66-X (X=$NO_2$, $NH_2$, OH, NDC) photothermal catalysts are synthesized through ligand functionalization for the oxidation of low-concentration VOCs. Among them, the UiO-66-OH catalyst achieves the highest conversion up to 97% and 90% for toluene and benzene (initial concentrations were 0.075 mg/L for toluene and 0.064 mg/L for benzene, respectively, a WHSV of 30000 mL/(g·h)), respectively, surpassing the reported photothermal catalysts such as metal oxides and noble-metal-loaded semiconductors. It also maintains excellent stability over five cycles. The introduction of hydroxyl groups in the ligands optimizes the electron structure and LMCT effects in UiO-66, narrowing the band gap and facilitating the electron transfer from ligand to metal center, thus effectively enhancing light absorption and improving electron-hole separation efficiency. Meanwhile, hydroxyl introduction markedly promotes the concentration of oxygen vacancies and significantly enhances the photothermal effect. Such impressive performance is attributed to the synergy of thermal catalysis involving highly active $O_{latt}$ and photocatalysis involving $\cdot O_2^-$ and $h^+$. The increased

oxygen vacancies enhance the activity of $O_{latt}$, facilitate the oxygen adsorption/activation and the generation of $\cdot O_2^-$. $O_{latt}$ mainly initiates C–H oxidation, $\cdot O_2^-$ and $h^+$ induce aromatic ring cleavage, enabling complete mineralization of toluene and benzene into $CO_2$ and $H_2O$. This work not only presents the potential of MOFs as efficient photothermal catalysts for the oxidation of low-concentration VOCs but also shows prospects on facile modulation of electron structure to enhance the photothermal properties of MOFs by ligand engineering.

## Supporting Materials

Supporting materials related to this article can be found at https://doi.org/10.15541/jim20250157.

## References:


[1] HE C, CHENG J, ZHANG X, *et al*. Recent advances in the catalytic oxidation of volatile organic compounds: a review based on pollutant sorts and sources. *Chemical Reviews*, 2019, **119(7):** 4471.

[2] MARINO E, CARUSO M, CAMPAGNA D, *et al*. Impact of air quality on lung health: myth or reality? *Therapeutic Advances in Chronic Disease*, 2015, **6(5):** 286.

[3] HUANG H B, XU Y, FENG Q Y, *et al*. Low temperature catalytic oxidation of volatile organic compounds: a review. *Catalysis Science & Technology*, 2015, **5(5):** 2649.

[4] ELIMIAN E A, ZHANG M, SUN Y, *et al*. Harnessing solar energy towards synergistic photothermal catalytic oxidation of volatile organic compounds. *Solar RRL*, 2023, **7(14):** 2300238.

[5] YANG Y, ZHAO S H, CUI L F, *et al*. Recent advancement and future challenges of photothermal catalysis for VOCs elimination: from catalyst design to applications. *Green Energy & Environment*, 2023, **8(3):** 654.

[6] MA X L, WANG W L, SUN C G, *et al*. Adsorption performance and kinetic study of hierarchical porous Fe-based MOFs for toluene removal. *Science of the Total Environment*, 2021, **793:** 148622.

[7] CHEN R F, YAO Z X, HAN N, *et al*. Insights into the adsorption of VOCs on a cobalt-adeninate metal-organic framework (bio-MOF-11). *ACS Omega*, 2020, **5(25):** 15402.

[8] LV S W, LIU J M, LI C Y, *et al*. Two novel MOFs@COFs hybrid-based photocatalytic platforms coupling with sulfate radical-involved advanced oxidation processes for enhanced degradation of bisphenol A. *Chemosphere*, 2020, **243:** 125378.

[9] ZHANG J H, HU Y, QIN J X, *et al*. $TiO_2$-UiO-66-$NH_2$ nanocomposites as efficient photocatalysts for the oxidation of VOCs. *Chemical Engineering Journal*, 2020, **385:** 123814.

[10] WU X P, GAGLIARDI L, TRUHLAR D G. Cerium metal-organic framework for photocatalysis. *Journal of the American Chemical Society*, 2018, **140(25):** 7904.

[11] HEU R, ATEIA M, YOSHIMURA C. Photocatalytic nanofiltration membrane using Zr-MOF/GO nanocomposite with high-flux and anti-fouling properties. *Catalysts*, 2020, **10(6):** 711.

[12] KIM H G, CHOI K, LEE K, *et al*. Controlling the structural robustness of zirconium-based metal organic frameworks for efficient adsorption on tetracycline antibiotics. *Water*, 2021, **13(13):** 1869.

[13] NAIK T S S K, SINGH S, PAVITHRA N, *et al*. Advanced experimental techniques for the sensitive detection of a toxic bisphenol A using UiO-66-NDC/GO-based electrochemical sensor. *Chemosphere*, 2023, **311:** 137104.

[14] MA Y L, LI A R, WANG Z H, *et al*. Preparation of UiO-66-type adsorbents for the separation of $SO_2$ from flue gas. *Adsorption*, 2024, **30(3):** 377.

[15] LUCATERO E, BASHIRI R, SO M C. Synthesis, characterization, and evaluation of metal–organic frameworks for oxidative desulfurization: an integrated experiment. *Journal of Chemical Education*, 2024, **101(8):** 3428.

[16] YOU X Q, LI Y, MO H R, *et al*. Theoretical studies on Lennard-Jones parameters of benzene and polycyclic aromatic hydrocarbons. *Faraday Discussions*, 2022, **238:** 103.

[17] ZHAO Y, WANG Y, WANG X Y, *et al*. Recent progress of photothermal therapy based on conjugated nanomaterials in combating microbial infections. *Nanomaterials*, 2023, **13(15):** 2269.

[18] MOGHADDAM Z S, KAYKHAII M, KHAJEH M, *et al*. Synthesis of UiO-66-OH zirconium metal-organic framework and its application for selective extraction and trace determination of thorium in water samples by spectrophotometry. *Spectrochimica Acta Part A: Molecular and Biomolecular Spectroscopy*, 2018, **194:** 76.

[19] NGUYEN V H, PHAM A L H, NGUYEN V H, *et al*. Facile synthesis of bismuth(III) based metal-organic framework with difference ligands using microwave irradiation method. *Chemical Engineering Research and Design*, 2022, **177:** 321.

[20] WRIGHT S, BARKLIE R C. EPR characterization of defects in monoclinic powders of $ZrO_2$ and $HfO_2$. *Materials Science in Semiconductor Processing*, 2006, **9(6):** 892.

[21] ZHANG Y T, CHENG C, ZHOU Z H, *et al*. Surface hydroxylation during water splitting promotes the photoactivity of $BiVO_4$(010) surface by suppressing polaron-mediated charge recombination. 2023, **14(40):** 9096.

[22] WU H, CHUA Y S, KRUNGLEVICIUTE V, *et al*. Unusual and highly tunable missing-linker defects in zirconium metal-organic framework UiO-66 and their important effects on gas adsorption. *Journal of the American Chemical Society*, 2013, **135(28):** 10525.

[23] BAKRADZE G, JEURGENS L P H, MITTEMEIJER E J. Valence-band and chemical-state analyses of Zr and O in thermally grown thin zirconium-oxide films: an XPS study. *The Journal of Physical Chemistry C*, 2011, **115(40):** 19841.

[24] CHI M Y, SUN X N, SUJAN A, *et al*. A quantitative XPS examination of UV induced surface modification of $TiO_2$ sorbents for the increased saturation capacity of sulfur heterocycles. *Fuel*, 2019, **238:** 454.

[25] JIANG Y, NING H Y, TIAN C G, *et al*. Single-crystal $TiO_2$ nanorods assembly for efficient and stable cocatalyst-free photocatalytic hydrogen evolution. *Applied Catalysis B: Environmental*, 2018, **229:** 1.

[26] LIU L Z, HUANG H W, CHEN F, *et al*. Cooperation of oxygen vacancies and 2D ultrathin structure promoting $CO_2$ photoreduction performance of $Bi_4Ti_3O_{12}$. *Science Bulletin*, 2020, **65(11):** 934.

[27] IBRAHIM D A H, HAIKAL D R R, ELDIN R S, *et al*. The role of free-radical pathway in catalytic dye degradation by hydrogen peroxide on the Zr-based UiO-66-$NH_2$ MOF. *ChemistrySelect*, 2021, **6(42):** 11675.

[28] MERKEL P B, LUO P, DINNOCENZO J P, *et al*. Accurate oxidation potentials of benzene and biphenyl derivatives *via* electron-transfer equilibria and transient kinetics. 2009, **74(15):** 5163.

[29] LIN H X, LONG J L, GU Q, *et al*. *In situ* IR study of surface hydroxyl species of dehydrated $TiO_2$: towards understanding

pivotal surface processes of $TiO_2$ photocatalytic oxidation of toluene. *Physical Chemistry Chemical Physics*, 2012, **14(26):** 9468.

[30] WANG F Z, LI W J, GU S N, *et al*. Fabrication of $FeWO_4$@$ZnWO_4$/ZnO heterojunction photocatalyst: synergistic effect of $ZnWO_4$/ZnO and $FeWO_4$@$ZnWO_4$/ZnO heterojunction structure on the enhancement of visible-light photocatalytic activity. *ACS Sustainable Chemistry & Engineering*, 2016, **4(12):** 6288.

[31] MO S P, LI J, LIAO R Q, *et al*. Unraveling the decisive role of surface $CeO_2$ nanoparticles in the Pt-$CeO_2$/$MnO_2$ hetero-catalysts for boosting toluene oxidation: synergistic effect of surface decorated and intrinsic O-vacancies. *Chemical Engineering Journal*, 2021, **418:** 129399.

[32] MO S P, ZHANG Q, LI J Q, *et al*. Highly efficient mesoporous $MnO_2$ catalysts for the total toluene oxidation: oxygen-vacancy defect engineering and involved intermediates using *in situ* DRIFTS. *Applied Catalysis B: Environmental*, 2020, **264:** 118464.

[33] CHEN L C, CHEN P, WANG H, *et al*. Surface lattice oxygen activation on $Sr_2Sb_2O_7$ enhances the photocatalytic mineralization of toluene: from reactant activation, intermediate conversion to product desorption. *ACS Applied Materials & Interfaces*, 2021, **13(4):** 5153.

# 配体羟基改性增强 UiO-66 的光热催化氧化 VOCs 性能

陈笑晨[1,2], 王 阳[2], 杨 彬[1], 王 敏[2], 阿博涵[2], 王 蔓[2], 张玲霞[1,2]

(1. 国科大杭州高等研究院 化学与材料科学学院, 杭州 310024; 2. 中国科学院 上海硅酸盐研究所, 上海 200050)

**摘 要:** 在室内和工业环境中, 高效去除低浓度挥发性有机化合物(VOCs)依然是一个重大挑战。金属有机框架(MOFs)对低浓度 VOCs 具有优异的吸附富集能力, 是一种有潜力的氧化催化剂。本研究通过在配体中引入羟基, 合成了 UiO-66-OH 催化剂, 其对低浓度 VOCs(甲苯质量浓度 0.075 mg/L, 苯质量浓度 0.064 mg/L, 空速(WHSV) 30000 mL/(g·h))表现出优异的光热催化氧化性能, 对甲苯和苯的转化率分别达到了 97%和 90%, 优于已报道的金属氧化物和贵金属光热催化剂。其优异的催化活性主要归因于热催化与光催化的协同效应。配体羟基化优化了 UiO-66 的电子结构及配体-金属-电荷转移(LMCT)效应, 从而增强了光吸收能力, 提高了电子-空穴分离效率和光热性能。同时, 引入羟基还促进了氧空位的生成, 有利于 $O_2$ 吸附活化, 生成的超氧自由基($\cdot O_2^-$)为主要活性氧物种。本研究不仅展示了 MOFs 在低浓度 VOCs 光热催化氧化中的应用潜力, 也提供了一种通过配体工程调控电子结构来提升 MOFs 光热性能的有效策略。

**关 键 词:** 挥发性有机化合物; 低浓度; 金属有机框架; 光热催化; 配体-金属电荷转移效应

**中图分类号:** TQ134 **文献标志码:** A **文章编号:** 1000-324X(2026)05-0663-10

**Supporting Materials**

# Ligand-hydroxylated UiO-66 for Enhanced Photothermally Catalytic VOCs Oxidation

CHEN Xiaochen[1,2], WANG Yang[2], YANG Bin[1], WANG Min[2], A Bohan[2], WANG Man[2], ZHANG Lingxia[1,2]

(1. School of Chemistry and Materials Science, Hangzhou Institute for Advanced Study, University of Chinese Academy of Sciences, Hangzhou 310024, China; 2. Shanghai Institute of Ceramics, Chinese Academy of Sciences, Shanghai 200050, China)

## S1 Characterizations

X-ray diffraction (XRD) patterns were collected by a Rigaku D/Max 2200PC X-ray diffractometer using Cu K$\alpha$ ($\lambda$=0.154 nm) at a scanning rate of 4 (°)/min and a 2$\theta$ range of 5°–60°. Fourier transformed infrared (FT-IR) spectra were recorded in the range of500–4000 $cm^{-1}$ using KBr pellets. The BET surface areas and porosity characteristics of both pristine UiO-66 and UiO-66-OH were measured using a Micromeritics ASAP 2460 surface and pore size analyzer through $N_2$ adsorption/ desorption at 77 K. Scanning electron microscopy (SEM) was performed on a Thermoscientific Quattro S field emission microscope at an accelerating voltage of 2 kV. X-ray photoelectron spectroscopy (XPS) measurements were carried out on a Thermo Scientific K-Alpha X-ray photoelectron spectrometer using Al K$\alpha$ radiation ($h\nu$=1486.6 eV) and setting C1s energy to 284.8 eV to calibrate the binding energy. A Bruker A300 spectrometer was used to record electron paramagnetic resonance (EPR) spectra. A Shimadzu UV-3600 spectrometer was used to acquire UV-Vis absorption spectra with $BaSO_4$ as reflectance standard. A Edinburgh FLS1000 fluorescence spectrophotometer with an excitation wavelength of 395 nm was used to obtain photoluminescence (PL) spectra. Mott-Schottky analysis was conducted at a direct current potential range from –1 to 1 V with an alternating current coupling with a frequency amplitude of (1000±100) Hz.

## S2 Catalytic performance

The photothermal catalytic performance of the catalysts was assessed using a custom-designed continuous flow reactor, with toluene or benzene serving as probe VOCs and a compressed gas mixture containing 20% (in volume) $O_2$ and 80% (in volume) $N_2$ was employed as oxygen source for the reactions. A Xe lamp (CEL-HXF300) with an intensity of 300 $mW/cm^2$ was used as light source. Due to the photothermal effect, the surface temperatures of UiO-66 and UiO-66-OH were measured to be approximately 60 and 115 ℃, respectively. In a standard test, 100 mg of catalyst was loaded into the reactor, and a gas mixture containing 0.075 mg/L for toluene and 0.064 mg/L for benzene in air was introduced at a flow rate of 50 mL/min, corresponding to a weight hourly space velocity (WHSV) of 30000 mL/(g·h). The concentrations of toluene, benzene and $CO_2$ in the effluent were continuously monitored using a gas chromatograph (GC-9790II, Fuli, China) equipped with two flame ionization detectors (FID) and a methanation furnace.

The thermocatalytic performance of the catalysts was measured in a continuous fixed-bed reactor in dark. The reaction temperature was controlled by an electrothermal furnace and other reaction conditions were the same as in PTC reaction.

The conversion rate of toluene or benzene was calculated using equation as follows:

$$\text{Conversion rate} = \frac{C_0 - C_t}{C_0} \times 100\% \qquad \text{(S1)}$$

where $C_0$ represents the initial concentration of toluene (0.075 mg/L) or acetaldehyde (0.064 mg/L), and $C_t$ denotes the concentration of remaining toluene or benzene at a given reaction time $t$.

Active species trapping experiments were performed using $AgNO_3$, triethanolamine (TEOA), p-benzoquinone (BQ), furfuryl alcohol (FFA) and isopropanol (IPA) as specific radical scavengers for $e^-$, $h^+$, $\cdot O_2^-$, $^1O_2$ and ·OH, respectively[S1]. In a typical process, 0.5 mmol of each scavenger was dissolved in 5 mL of ethanol. Subsequently, 100 mg of catalyst was added into the solution, and the mixture was sonicated for 30 min to form a uniform suspension. The suspension was then dried at 60 ℃ overnight, and the treated catalysts were subjected to photothermal catalytic tests.

## S3 *In-situ* Fourier transform infrared spectra

The *in-situ* Fourier transform infrared (FT-IR) spectra was recorded by a Nicolet iS10 spectrometer with an

HgCdTe (MCT) detector. Light was provided by an Xe lamp (CEL-HXF300). The catalyst was pretreated in $N_2$ at 60 ℃ for 30 min and then cooled to room temperature. The *in-situ* FT-IR spectrum of the catalyst was collected as background. Then, benzene or toluene vapors were introduced in dark to reach adsorption equilibrium. Subsequently, a gas mixture (20% oxygen, 80% nitrogen) was introduced at a rate of 50 mL/min. Finally, the light was applied. After the background collection, spectra were collected every 5 min throughout the process.

**Table S1 Hydrothermal conditions for the synthesis of UiO-66 and UiO-66-X catalysts**

| Sample | Temperature/℃ | Time/h |
|---|---|---|
| UiO-66 | 120 | 24 |
| UiO-66-NDC | 120 | 24 |
| UiO-66-$NO_2$ | 120 | 24 |
| UiO-66-$NH_2$ | 120 | 12 |
| UiO-66-OH | 80 | 12 |

**Table S2 Performance comparison of relevant catalysts on benzene and toluene oxidation**

| Catalyst | VOC | Concentration/(mg·L$^{-1}$) | Catalyst amount/mg | Light intensity/(mW·cm$^{-2}$) | Conversion/% |
|---|---|---|---|---|---|
| Pt/$TiO_2$[S2] | Benzene | 0.96 | 100 | 300 | 84.5 |
| Pt/g-$C_3N_4$[S3] | Benzene | 0.96 | 150 | 500 | 95 |
| This work | Benzene | 0.064 | 100 | 300 | 90 |
| $MnO_x$-$TiO_2$[S4] | Toluene | 0.02 | 500 | – | 72 |
| $TiO_2$-UiO-66-$NH_2$[9] | Toluene | 0.094 | 100 | 50 | 73 |
| Pt/$MnO_x$[S5] | Toluene | 0.75 | 100 | 200 | 90 |
| This work | Toluene | 0.075 | 100 | 300 | 97 |

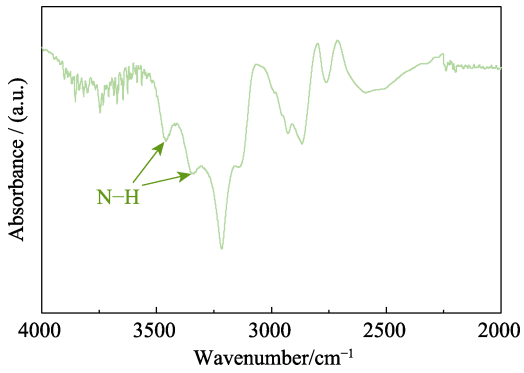


Fig. S1 FT-IR spectrum of UiO-66-$NH_2$ in the range of 2000–4000 cm$^{-1}$

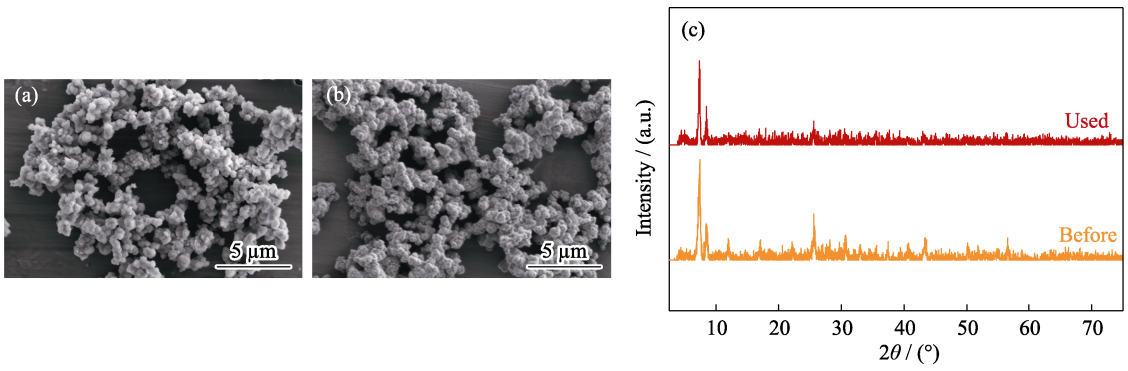


Fig. S2 (a, b) SEM images and (c) XRD patterns of UiO-66-OH (a) before and (b) after five catalytic cycles

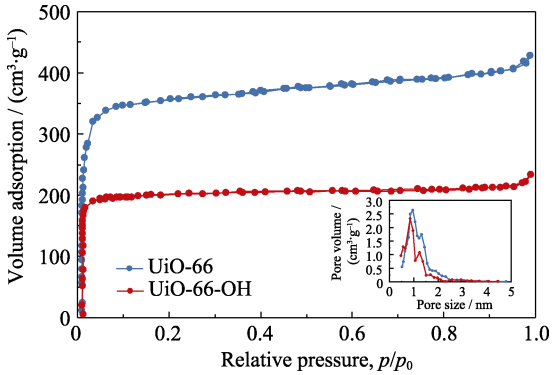


Fig. S3　$N_2$ adsorption-desorption isotherms at 77 K with inset showing pore-size distributions of UiO-66 and UiO-66-OH

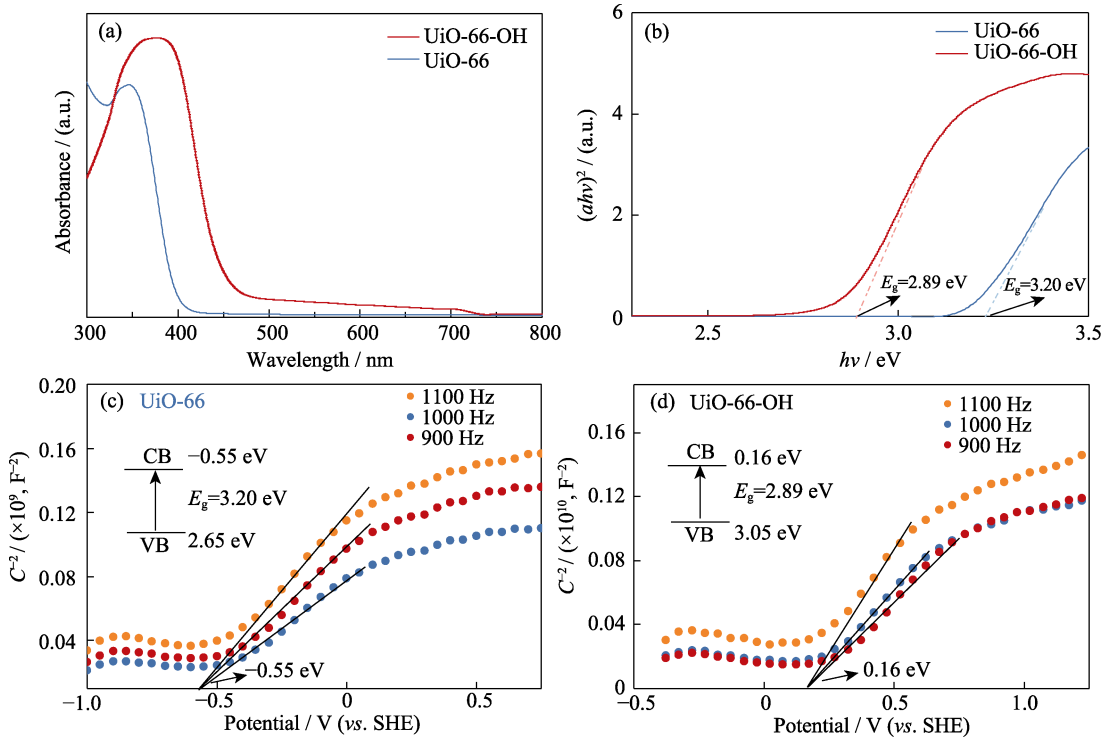


Fig. S4　(a) UV-Vis absorption spectra; (b) Tauc plots; (c, d) Mott-Schottky plots of (c) UiO-66 and (d) UiO-66-OH

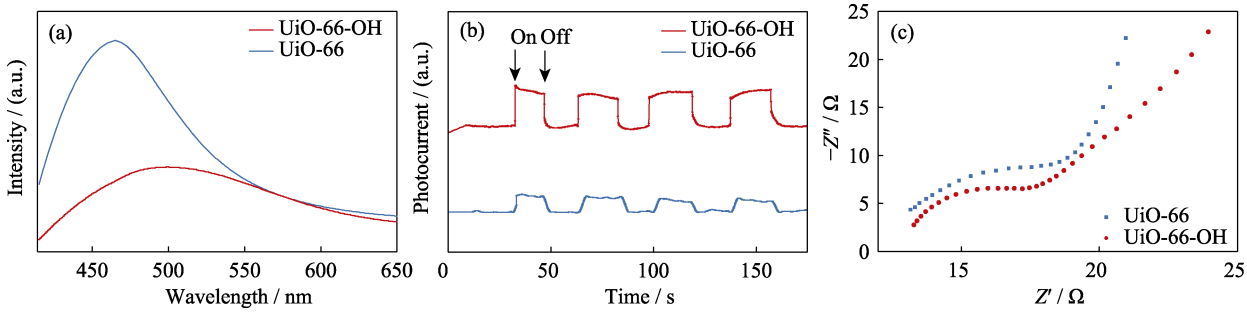


Fig. S5　(a) PL spectra, (b) photocurrent response spectra and (c) Nyquist plots of UiO-66 and UiO-66-OH

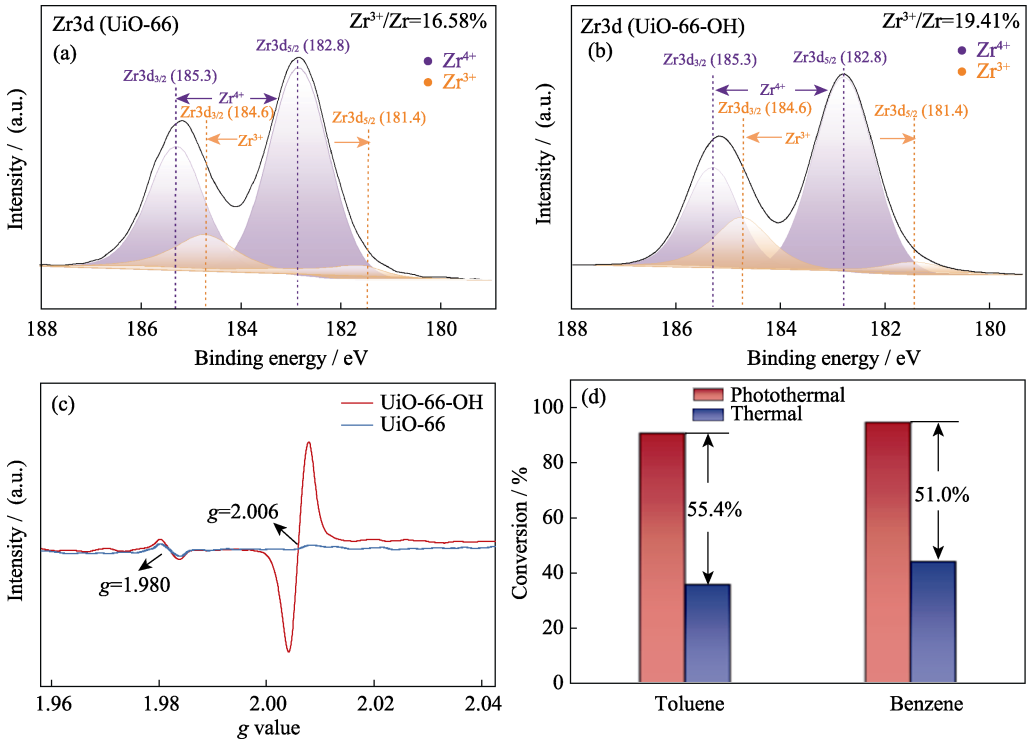


Fig. S6 (a, b) Zr3d XPS spectra of (a) UiO-66 and (b) UiO-66-OH, (c) EPR spectra of UiO-66 and UiO-66-OH, and (d) comparison of toluene and benzene conversion by photothermal catalysis and thermal catalysis

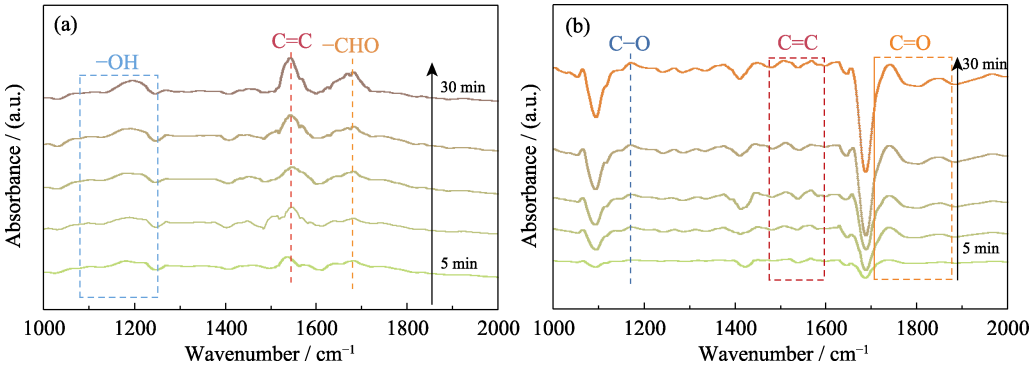


Fig. S7 *In-situ* FT-IR spectra of UiO-66 for oxidation of (a) toluene and (b) benzene under $O_2$ and irradiation conditions

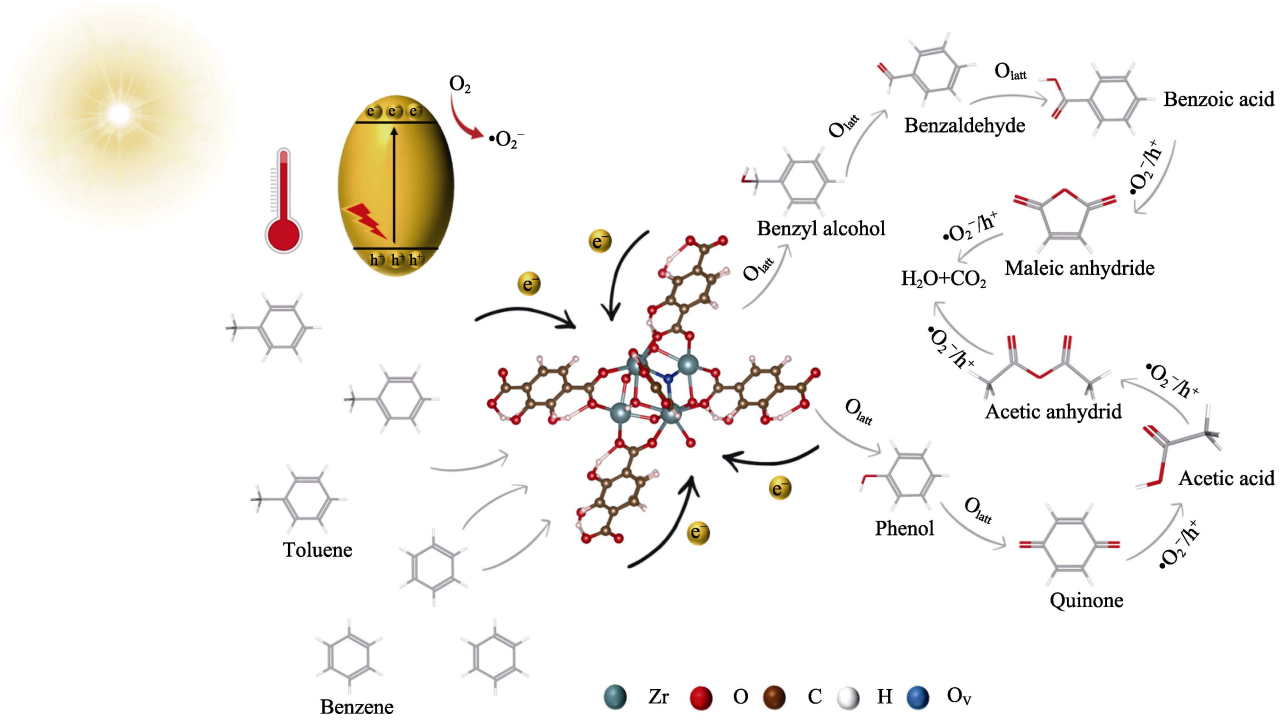


Fig. S8　Possible oxidation reaction pathways of toluene and benzene on UiO-66-OH

# References:


[S1] XIAO S N, PAN D L, LIANG R, *et al*. Bimetal MOF derived mesocrystal $ZnCo_2O_4$ on rGO with high performance in visible-light photocatalytic NO oxidization. *Applied Catalysis B: Environmental*, 2018, **236:** 304.

[S2] REN L, LI Y Z, LIU H H, *et al*. UV–Vis–infrared light-driven photothermocatalytic synergetic effect leading to efficient benzene abatement by Pt supported on anatase $TiO_2$ with {001}facets. *ACS Applied Energy Materials*, 2020, **3(8):** 7920.

[S3] HUANG Z C, CAI X R, ZANG S H, *et al*. Strong metal support effect of Pt/g-$C_3N_4$ photocatalysts for boosting photothermal synergistic degradation of benzene. *International Journal of Molecular Sciences*, 2023, **24(7):** 6872.

[S4] LI M R, WANG Y H, FAN Y M, *et al*. Controllable synthesis various morphologies of 3D hierarchical $MnO_x$-$TiO_2$ nanocatalysts for photothermocatalysis toluene and NO with free-ammonia. *Journal of Colloid and Interface Science*, 2022, **608:** 3004.

[S5] YU E Q, LI J J, CHEN J, *et al*. Enhanced photothermal catalytic degradation of toluene by loading Pt nanoparticles on manganese oxide: photoactivation of lattice oxygen. *Journal of Hazardous Materials*, 2020, **388:** 121800.